

This is the accepted manuscript made available via CHORUS. The article has been published as:

Role of catch bonds in actomyosin mechanics and cell mechanosensitivity

Franck J. Vernerey and Umut Akalp

Phys. Rev. E **94**, 012403 — Published 11 July 2016

DOI: [10.1103/PhysRevE.94.012403](https://doi.org/10.1103/PhysRevE.94.012403)

The role of catch-bonds in acto-myosin mechanics and cell mechano-sensitivity

Franck J. Vernerey* and Umut Akalp

Department of Mechanical Engineering, University of Colorado, Boulder

(Dated: June 13, 2016)

We propose a novel mechanism of adherent cell mechano-sensing, based on the idea that the contractile acto-myosin machinery behaves as a catch-bond. For this, we construct a simplified model of the acto-myosin structure that constitute the building block of stress fibers and express the stability of cross-bridges in terms of the force-dependent bonding energy of the acto-myosin bond. Consistent with experimental measurements, we then consider that the energy barrier of the acto-myosin bond increases for tension and show that this response is enough to explain the force-induced stabilization of an SF. Further numerical simulations at the cellular level show that the catch-bond hypothesis can help in understanding and predict the sensitivity of adherent cells to substrate stiffness.

The contraction of adherent cells is a phenomenon that plays a large role in many biological processes such as morphogenesis [1], wound contraction [2], stem cell differentiation [3] and the development of many diseases [4]. The molecular mechanisms by which cells generate motion and force depend on a series of highly coordinated events occurring in both the cytoskeleton and at the cell membrane. Of particular importance are the contractile elements of the cytoskeleton, made of stress fibers (SF) [5, 6]. These filaments, that assemble from proteins present in the cytosol (including mainly globular actin and myosin) generally anchor to the cell substrate via focal adhesions and can ultimately span the entire length of the cell. Importantly, these filaments are capable of sustaining appreciable levels of contraction, which they owe to the underlying acto-myosin machinery powered by ATP. In the past decade, a number of studies have shown that both SF density and contraction in adherent cells were sensitive to the mechanical environment [3, 7, 8]; a stiffer environment generally promotes a denser, stronger cytoskeleton and eventually cell spreading [9]. Understanding the fundamental origin of these behaviors has motivated a number of theoretical studies, from the cellular to the molecular level. A line of thought has been to view cells as contraction dipoles [10] that could sense the compliance of their substrate and accordingly polarize by minimizing their deformation energy [11]. Others have considered the contractile cytoskeleton as an active material in which filament stability is promoted by tension [12–14]. The molecular origin of this phenomenon was explained by the presence of signaling pathways that induced a positive feedback for SF stabilization with force [15]. Other classes of models, based on cross-bridge dynamics [16] have also been used to explain the effect of tension on cytoskeleton reorganization under static and cyclic conditions [17]. A more

thorough review of existing models was discussed in [18]. While bio-chemical signaling has often been argued as an possible factor, the way by which SFs stabilize with tension still remains an open question. In this paper, we invoke a well-known mechano-sensitive element used by biology, the catch bond, to explain both the force-stabilization response of SFs and the development of intricate cytoskeletal architectures in adherent cells. Such bonds are typically found on the membrane of leucocytes and bacteria [19] and act to strengthen the adhesion with a solid substrate in the presence of an external force. They may also play the role of rigidity sensors on the surface of adherent cells, through specific membrane receptors and notably the $\alpha_5\beta_1$ integrin [20]. Contrary to the conventional slip bonds whose detachment rate increases with force as described by Bell’s law [21], catch bonds are able to extend their lifetime under the application of a small to moderate force. While the origin of this behavior may be complex at the molecular scale (arising from mechano-chemical interactions or multiple force-dependent bond states for instance [22, 23]), the overall response of catch bonds is quite robust across biological systems. Of particular interest in the case of SFs is the finding, notably by Guo et al. [24] that the actin-myosin complex does display a catch-bond behavior, with a maximum stabilizing force around $6pN$. This observation is further confirmed by Capitanio et al. [25] who measured a force-induced reduction in the detachment rate of myosin from actin after its working stroke for forces ranging between 0 and $6pN$ **at high ATP concentration** and Reconditi et al. [26] who found similar trends in the mechanics of muscle fibers. Alternatively, there may be other types of mechano-sensitive mechanisms in the SF machinery, which could include, for instance, a force-dependent transition among the different nucleotide states of myosin during its mechano-chemical cycle on actin. These considerations, along with the data from Guo et al. [24] clearly indicate the possibility of catch-bond within SFs. To investigate this hypothesis, we propose to explore whether the existence of a *catchy* acto-myosin bond could be at the origin of (a) the force and stiffness-induced SF stabilization and (b) the com-

* Corresponding Author: franck.vernerey@colorado.edu ; Also in the Program of Material Science and Engineering, University of Colorado, Boulder

plex acto-myosin cytoskeleton architecture observed in a majority of adherent cells. For this, we proceed in two steps; first, we introduce an active visco-elastic model of SF that incorporates the idea of force-induced stabilization of cross-bridges. Second, we propose a simple model of the acto-myosin cytoskeleton of adherent cells, made of a random assembly of force-sensitive SFs. A computational procedure is introduced to predict the contractile behavior and cytoskeleton architecture of adherent cells laying on beds of micro-posts. Results are discussed in the light of experimental data from the literature.

I. MODELING STRESS FIBERS AS ACTIVE VISCO-ELASTIC FILAMENTS

As shown in Fig. 1, SFs are generally viewed as bundles of polar actin filaments which, depending on maturity, can display a periodic appearance associated with the presence of organized repeating structure of myosin and alpha-actinin molecules [27]. Myosin filaments possess proteins domains, or heads, that have the ability to execute power strokes towards the positive end of an actin filament. This operation, collectively, results in an overall shortening of the acto-myosin assembly at a speed that can vary depending on the type of myosin (see discussion in appendix A.3. and Table 1). Based on these observations, we propose to model a SF control segment as a parallel assembly of three key elements (Fig. 1): (a) a contractile element that captures the change Δd_s in SF length due to the sliding of myosin heads on actin filaments at a rate $\Delta \dot{d}_s = v_s$ (here v_s is negative) (b) an elastic element of stiffness k [24, 28] characterizing the elasticity of cross-bridges and whose stretch Δd_e is recoverable upon unloading and (c) a bond element that represents the strength of the actin-myosin complex. Note that initially, the segment is in an optimal configuration, i.e., active actin sites and myosin cross-bridges perfectly overlap and a deviation from this length is given by $\Delta d = \Delta d_s + \Delta d_e$. Now assuming that the overlap ratio decreases linearly with sliding Δd_s , the maximum number of cross-bridges that can be formed during contraction is estimated as

$$N(d_s) = N_f N_x (1 - \Delta d_s / \Delta d_s^{max}) \quad (1)$$

where N_f is the number of myosin minifilaments in the control segment while N_x is the number of myosin heads per myosin filament. In this work, we choose $\Delta d_s^{max} = \ell/4$ [29] as the distance at which the actin-myosin filaments generally cease to overlap. This relationship is at the origin of the *length-tension relation* in muscle mechanics [30].

A. Active visco-elastic model

The dynamics and force generation in acto-myosin units have traditionally been studied using the sliding

filament theory [16, 31, 32]. Based on the detailed kinetics and transition between different states of myosin motors during their working cycle, the theory enables the determination of the fraction of attached cross-bridges on an actin filament as well as their velocity and working force in terms of external conditions. Although such an approach would provide a good starting point to our derivation, its level of details may divert us from our main objective, i.e., understand the role of acto-myosin catch bond on cell mechano-sensitivity. We therefore keep this alternative for future work and instead propose a simplified approach which consists of investigating the equilibrium of a SF segment by considering the balance of entropy, conservative and non-conservative forces within the acto-myosin assembly as it is subjected to an external force F_e . To describe the former two contributions, we build a Gibbs free energy functional in the form: $G = U - TS$ where U , S and T are the stored internal energy, entropy and thermodynamic temperature in the control segment, respectively. To evaluate S , we first investigate the number of possible bond configurations in the attached (A) and detached (D) state amongst the available acto-myosin bonds. If we define $0 \leq \eta \leq 1$ as the ratio N_A/N of attached bonds (N_A being the number of attached bonds), the entropy of the system reads $S = -k_B N(\Delta d_s) [\eta \ln(\eta) + (1 - \eta) \ln(1 - \eta)]$ where k_B is the Boltzmann constant. The internal energy of the unit is then composed of two terms: the stored elastic energy $\frac{1}{2} k \Delta d_e^2$ and the adhesion energy E_b stored in attached bonds. This yields $U = \eta N(\Delta d_s) (k \Delta d_e^2 / 2 - E_b)$. The total Gibbs energy functional can then be written:

$$\begin{aligned} \mathcal{E}[\eta, \Delta d_e] = & k_B T N(\Delta d_s) [\eta \ln(\eta) + (1 - \eta) \ln(1 - \eta)] \\ & + \frac{1}{2} \eta N(\Delta d_s) k \Delta d_e^2 - \eta N(\Delta d_s) E_b \\ & - \int_{\Delta d_e} F_e \delta \Delta d_e. \end{aligned} \quad (2)$$

The Rayleigh dissipation potential can similarly be written in term of the sliding velocity v_s and the external force F_e as:

$$\mathcal{D}[v_s] = \frac{1}{2} N \eta \mu v_s^2 - F_e v_s. \quad (3)$$

The term $N \eta \mu$ is to be interpreted as the overall viscosity between actin and myosin filaments while μ is the viscosity arising from a single cross-bridge. The latter can be considered as a lumped representation of a number of physical phenomena occurring during the working stroke of a myosin head, i.e., size and rate of the motor swing as well as how the rates of attachment and detachment of the myosin head on actin depend on force [33, 34]. The consideration of each individual mechanism, which is beyond the scope of this work, would therefore likely yield a non-linear viscosity that depends on force in a more complex fashion than presented here. Nevertheless, the presented model, as it captures the main trends exhibited by the above phenomena, is sufficient for the

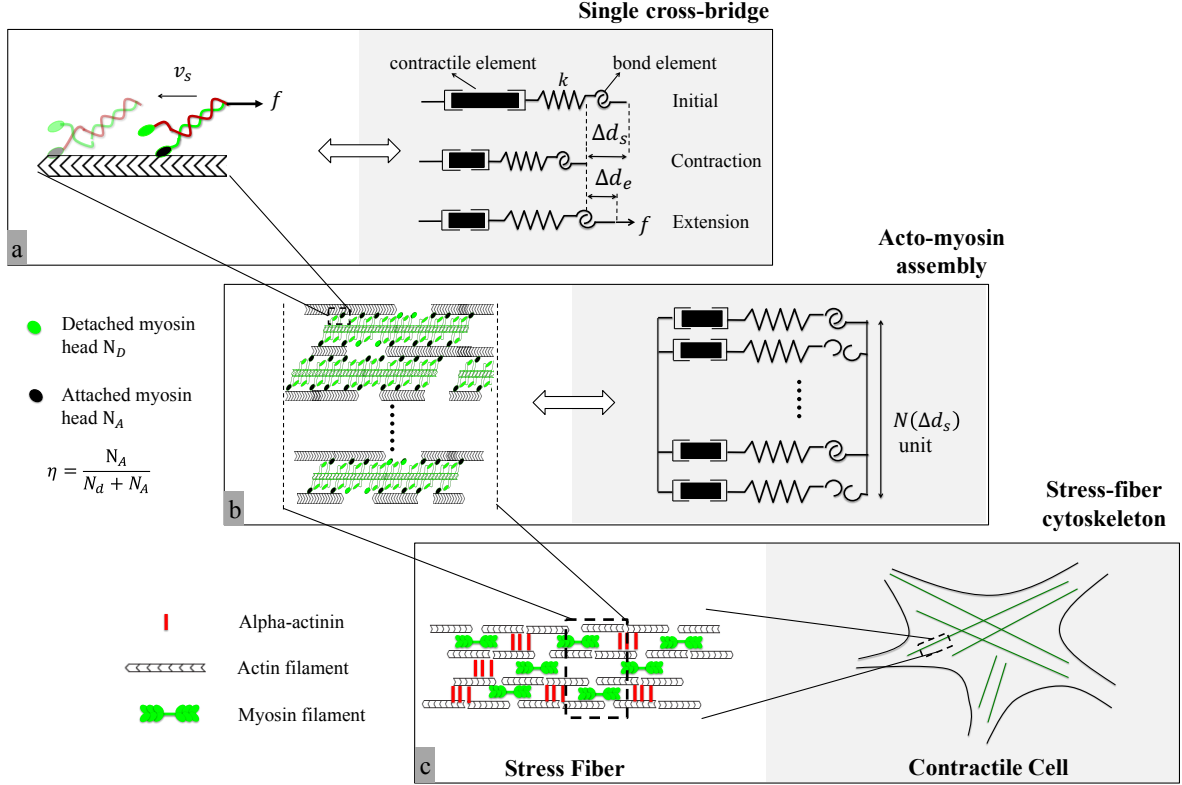


FIG. 1. Overview of the contractile machinery of adherent cells from the molecular to the micron scale. (a) At the molecular scale, the dynamics of contraction starts from the motion of myosin motors that can attach to actin filaments and walk along them via coordinated configurational changes of the myosin head powered by ATP. The stability of these cross-bridges is affected by the applied load f . In this study, this unit is modeled by a series of three elements comprised of a contractile element (whose contraction rate is v_s), a compliant element of stiffness k , that captures the elasticity of the cross-bridge and an "adhesive" element that represents the bond between actin and myosin. (b) A SF segment is primarily made of aligned and polarized actin filaments cross-linked by a series of thick actin myofilaments whose motion along the actin tracks is facilitated by the motion of cross-bridges. The overall SF contraction strain and force depend on the force generated by each individual myosin head and the number of attached acto-myosin bonds, whose fraction is represented by the variable η . This organization can be represented by a parallel assembly of single cross-bridge elements shown in (a) which may be in an attached and detached state. (c) Assembled in series, these segment make up SFs which constitute the main contractile element of adherent cells. SFs typically organize into a well aligned network whose elements can span a cell between two adhesion points. v_s is the sliding velocity, f is the external force against contraction, k is the acto-myosin bond stiffness, Δd_s is the contraction, Δd_e is the elastic stretch of the bond, η is the ratio of the number of attached cross-bridges to that of total available crossbridges $N(\Delta d_s)$ at contraction Δd_s .

present analysis. Finally, one now should specify the energy provided to the system by ATP hydrolysis in order to power the sliding of myosin heads on actin filaments. For this, we introduce the active force ζ produced by a single myosin molecule and compute the power produced in the control segment as:

$$\mathcal{A}[v_s] = N\eta\zeta v_s. \quad (4)$$

It is clear here that the term ζ is what drives the contractility of the acto-myosin unit and may be linked to the difference in chemical potential between ATP and its reaction products as discussed in [35]. The governing equation of our active acto-myosin filaments may then be obtained by balancing dissipation, energy release rate and active work. For this it is convenient to work with

the functional:

$$\mathcal{F}[\dot{\eta}, v_e, v_s] = \mathcal{D}[v_s] + \dot{\mathcal{E}}[\dot{\eta}, v_e] - \mathcal{A}[v_s]$$

whose minimization $\delta\mathcal{F}[\dot{\eta}, v_e, v_s] = 0$ leads to the equation:

$$(\delta_{\dot{\eta}}\mathcal{F})\delta\dot{\eta} + (\delta_{v_e}\mathcal{F})\delta v_e + (\delta_{v_s}\mathcal{F})\delta v_s = 0.$$

Enforcing that fact that the variations of $\dot{\eta}$, v_e and v_s are independent $\delta_{v_e}\mathcal{F}$, $\delta_{\dot{\eta}}\mathcal{F}$ and $\delta_{v_s}\mathcal{F}$ must all vanish, one can obtain the three Euler-Lagrange governing equations:

$$\eta N k \Delta d_e - F_e = 0, \quad (5)$$

$$E_b + k_B T \ln\left(\frac{\eta}{1-\eta}\right) = 0, \quad (6)$$

$$\mu v_s + \zeta - f = 0. \quad (7)$$

The first equation is interpreted as the mechanical equilibrium of the control segment, while the second denotes its chemical equilibrium (equality of the chemical potentials) of bonds in their attached and detached states. The last equation finally describes how the cross-bridge velocity is affected by the balance between the active force ζ and passive force $f = k\Delta d_e$. Interestingly, if one defines the natural (or maximal) sliding velocity as $v_s^0 = -\zeta/\mu$, Eq. (7) can be rewritten:

$$v_s = v_s^0 (1 - f/\zeta). \quad (8)$$

In the range $0 < f < \zeta$, this relation may therefore be thought of as a simplified (bi-linear) form of the velocity-tension relationship [36] that describes how the sliding velocity decreases if an opposing force f is applied to the acto-myosin unit. This expression is consistent with recent findings [25, 26] that the myosin stroke size (and hence its velocity) decreases with applied load. In this context, ζ can be interpreted as a stall force, i.e., the force that must be applied to a single cross-bridge to stop its motion. Experimental approaches have estimated its value to be around $5pN$ [37] in algal cells.

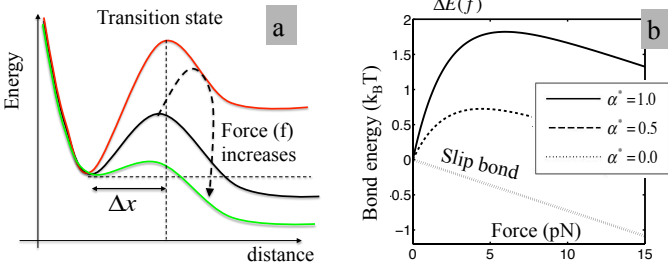


FIG. 2. (a) Energy landscape of the acto-myosin bond in the direction of applied force. The bond needs to go over the energy barrier (or transition state) in order to switch from its bound to unbound state. For a catch bond, the height of the energy barrier increases with moderate force until it starts decreasing for larger magnitude. This ultimately yields a force-induced stabilization of the bond. (b) Relationship between the height ΔE_b of the energy barrier and applied force as predicted by the Pereverzev and Prezhdo model [38] used in this study, for different values of bond catchiness α^* . The case $\alpha^* = 0$ corresponds to a slip bond response.

B. Acto-myosin catch-bonds

To complete the model, we now need to express the fact that the actin-myosin complex displays a catch-bond behavior. For this, consider the energy landscape of a single bond as depicted in Fig. 2a, in which ΔE is the energy barrier separating the bound and unbound states. Typically, the larger the energy barrier, the longer a bond can live under thermal fluctuations. When subjected to a tensile force f , the energy barrier of a conventional “slip bond” typically decreases according to Bell’s law

[21] as $E_b(f) = E_b^0 - f\Delta x$ where E_b^0 is the reference energy of the bond and $\Delta x \approx 3nm$ [39] is the width of the barrier. As shown in the literature [24, 25], acto-myosin complexes are temporarily stabilized when moderate pulling forces are applied, a response that can be interpreted as an temporary increase in the energy barrier ΔE_d with forces. Although a number of functions can be chosen to satisfy that criterion, we choose here the following two-parameter function originally proposed by Pereverzev and Prezhdo [38] as:

$$E_b(f) = E_b^0 + \alpha \left[1 - e^{-f/f_0} \right] - f\Delta x \quad (9)$$

where α measures the “catchiness” of the bond and f_0 is used to scale the force at which the bond stabilizes (Fig. 2b). We note that when $\alpha = 0$, the above expression degenerates to that of a slip bond following Bell’s law. In this study, we choose $E_0 = 4.8k_B T$, $f_0 = 2.2pN$ and explore a range of bond catchiness between 0 and $\alpha_{max} = 2.4k_B T$, in order to match a maximum stabilization at $\eta = 5\%$ [17] for a peak force of $6pN$ [24], consistent with the literature. A single value of bond stiffness k was further chosen, corresponding to non-muscle myosin (NMM) and smooth muscle myosin (Table 1). For this parameter, values reported in the literature are limited and very scattered, which motivated the discussion and parametric study provided in Appendix A.4. Overall, we show that the magnitude of k does affect the kinetics and forces generated by SF, but does not affect the main trends of its response discussed in the remainder of this manuscript. Using the expression for E_b in Eq. (6), one finds that the level η of cross-bridge attachment obeys:

$$E_b^0 + \alpha \left[1 - e^{-f/f_0} \right] - f\Delta x - k_B T \ln \left(\frac{\eta}{1 - \eta} \right) = 0. \quad (10)$$

C. Stress fiber mechano-sensitivity

Let us now assess the consequence of this model on the mechano-sensitivity of a SF control segment subjected to a constant external force F by investigating its stabilization via the fraction of attached bonds η . For clarity, we assume here that the SF does not contract during the application of the force (i.e. $v_s = 0$). In this case, η is directly calculated from (10) as

$$\eta(f) = \frac{e^{-E_b(f)/(k_B T)}}{1 + e^{-E_b(f)/(k_B T)}} \quad (11)$$

where the force in an attached acto-myosin bond is obtained from (5) as $f = F/(\eta N(\Delta d_s))$. This enables us to explore the force-induced activation of the SF as a function of bond catchiness $\alpha^* = \alpha/\alpha_{max}$. Fig. 3 therefore illustrates, for different values of bond catchiness α , how the variable η is affected by (a) the force f on a single acto-myosin bond and (b) the total force

$F = \eta N f$ on the acto-myosin assembly. Fig. 3a shows that for a slip bond ($\alpha^* = 0$), the steady state fraction η monotonically decreases with force as predicted by Bell's law while as α^* approaches unity, the fraction of attached bond becomes close to its maximum ($\approx 5\%$) for a critical force determined by $f_c = f_0 \ln\left(\frac{\alpha}{f_0 \Delta x}\right)$. We also observe a clear difference between the stability-force behavior for a single bond and the full segment as shown in Fig. 3b. Multiple bonds exhibit a cooperative behavior since for a given macroscopic force F , the force in individual bonds increases with decreasing η . As a result, we still see the force induced stabilization under the critical force $F_c = N\eta(f_c)f_c$ for $\alpha > 0$ but a catastrophic disassembly occurs for a larger force. Passed its maximum value F_c , the resisting force F therefore decreases quickly as cross-bridges become unstable and detach, a behavior is reminiscent of the fracture behavior of a fiber bundle, showing catastrophic disassembly at critical force [40].

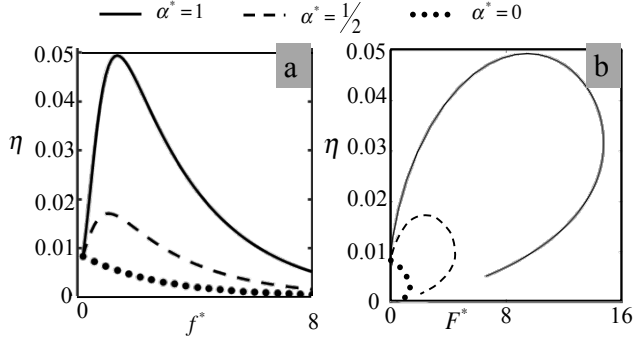


FIG. 3. Effect of (a) local (on a single cross-bridge) and (b) global (on the full SF segment) force on the fraction η of bound acto-myosin bonds in the SF segment in the absence of cell contraction ($v_s = 0$). Predictions are shown in the case of an acto-myosin slip bond $\alpha^* = 0$, moderate catch bond $\alpha^* = 0.5$ and strong catch bond $\alpha^* = 1$. These results clearly show the force-induced stabilization of the cross-bridges as the bond catchiness is increased (panel a). They also show a dramatic disassembly of the acto-myosin bundle when the applied force F^* reaches its critical value (panel b). $f^* = f/\zeta$ and $F^* = F/\zeta$.

We next explore the behavior of the same SF segment when it is allowed to contract against the load, i.e. cross-bridges slide on actin filaments at a velocity given by Eq. (8). In this context, Fig. 4 provides results regarding the time history of the contraction (top panels) and its steady state for different external forces (bottom panels). More specifically, the time response of the SF segment was investigated by plotting the fraction η (Fig. 4a) and the normalized acto-myosin force $f^* = f/\zeta$ (Fig. 4b) for three values of acto-myosin bond catchiness $\alpha^* = 0, \frac{1}{2}$ and 1, respectively. These results show that when the applied force F is moderate (F is smaller than a critical

value F_c determined above), bond catchiness promotes acto-myosin stability which yields an increase in the fraction of activated cross-bridges with α . One also sees that this activation monotonically increases in time as the segment contracts at a rate given by Eq. (8). However, once the force f per each cross bridge reaches its maximum value ζ , contraction ceases and the segment reaches its maximum contraction strain. The latter is sensitive to both applied force and bond catchiness as shown in Fig. 4c. On this figure, one indeed sees that the normalized segment contraction $\delta^* = \Delta d/\Delta d_{max}$ decreases with the amount of tension F^* . When $F^* = 0$, maximum SF shortening is reached while when the tension reaches its stalling value F_S (which corresponds to a cross-bridge force $f = \zeta$), no shortening is observed. One further notices that if the force increases to a critical value F_R , the force in each cross-bridge reaches its maximum capacity f_R (corresponding to the peak force of $6pN$) and the segment ruptures. In this process, we also note that bond catchiness plays a role in stabilizing the segment against external tension as it delays both the stalling and the rupture force significantly. We finally show in Fig. 4d the effect of applied force on the overall activation $a = \eta * N(\Delta d_s)/(N_x N_y)$ of attached crossbridges. Similarly to Fig. 3, in the case of a catch bond, we observe an obvious activation of the number of cross-bridges with external force until the force in an acto-myosin bond reaches its stalling (and rupture) value. For a slip bond however, the activation of the SF segment is negligible and quickly reaches its maximum capacity when a force is applied. Overall, these results point out that external tension is key to the activation and stabilization of a SF segment and that this response is strongly dependent on the catchiness of the acto-myosin bond.

Due to its biological relevance, we now investigate the model's prediction regarding the stiffness sensing capability of a SF; this can be done by considering a virtual experiment in which the control segment is attached to a rigid support on one end and to a compliant substrate, represented by a linear spring of stiffness K on the other (Fig. 5). Assuming that the spring is in its unstretched configuration when the SF is in its relaxed state ($\Delta d = 0$), the external force becomes $F = K\Delta d$. In Fig. 5(a&b), we show the time evolution of the fraction of active cross-bridges η and the contraction rate $v^* = v_s/v_s^0$ for an external stiffness $K = k/2$ and explore the effect of the bond catchiness on this process. As observed with the constant force, bond catchiness is a critical parameter for stiffness sensing; when $\alpha^* = 0$, activation is insensitive to stiffness, while for larger values of α^* , one sees a monotonic increase in SF activation with time, until it reaches a steady state. Interestingly, as bond catchiness increases, the model predicts a slow down of the contraction dynamics (Fig. 5b) as observed in experimental studies of contractile cells (See Fig. 7). This response may be attributed to the fact that a stronger catch bond induces larger forces f in acto-myosin bonds,

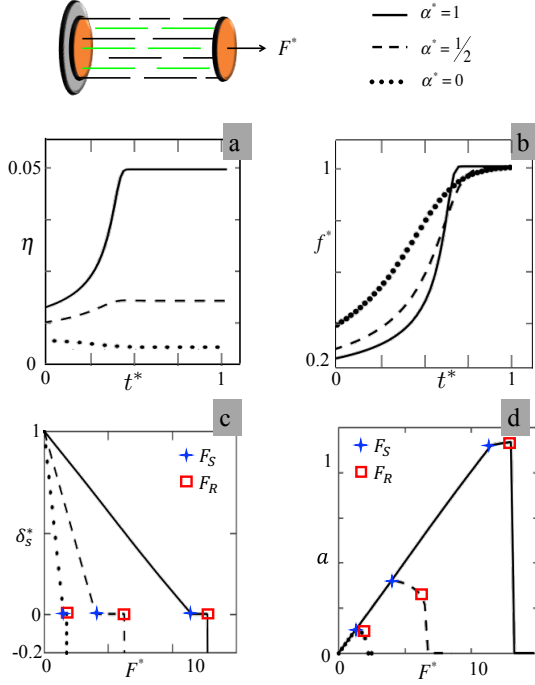


FIG. 4. Investigation of a SF segment as it is contracting under a constant load $F^* = F/\zeta$ for different values of normalized bond catchiness $\alpha^* = 0, 0.5$ and 1. **Top figures:** (a) Fraction of attached cross-bridge η and (b) force $f^* = f/\zeta$ on an active crossbridge as a function of time for $F^* = 1.2$. **Bottom figures:** (c) Normalized steady-state SF contraction $\delta_s^* = \Delta d_s / \Delta d_s^{max}$ and activation $a = \eta * N(\Delta d_s) / (N_x N_y)$ of an SF segment as a function of applied force F^* . The symbols + and □ indicate the points at which the SF segment stalls and ruptures, respectively.

which in turn yield smaller sliding velocities as predicted by Eq.(8). Beyond this dynamic response, external stiffness is also known to strongly influences SF contraction at steady state. In the model, the steady state corresponds to a vanishing sliding velocity $v_s = 0$, which translates, using Eq. (7), to the conditions that the force in acto-myosin bonds is $f = \zeta$. This implies, after a simple calculation and assuming that $\Delta d_s \gg \Delta d_e$, that contractile force is related to stiffness K by:

$$F^* = \frac{K^* \bar{\eta}}{K^* + \bar{\eta}} \quad (12)$$

where $F^* = F/(N\zeta)$, $K^* = K/k$ and $\bar{\eta} = \eta(f = \zeta)$. A graphical representation of this expression is given in Fig. 5c for different values of bond catchiness. This result shows that the SF contraction force increases sharply with external stiffness for small stiffness ($F^* \approx K^*$ as $K^* \rightarrow 0$) and asymptotically reaches the plateau $F_{max}^* = \bar{\eta}$ for stiffer environments (when $K^* \gg \bar{\eta}$). Since the value of $\bar{\eta}$ strongly depends on α^* , results show that stiffness sensitivity of the SF is highly dependent on bond catchiness: when α decreases, $\bar{\eta}$ diminishes until it reaches an unrealistically low activation value ($\bar{\eta} < 0.05\%$)

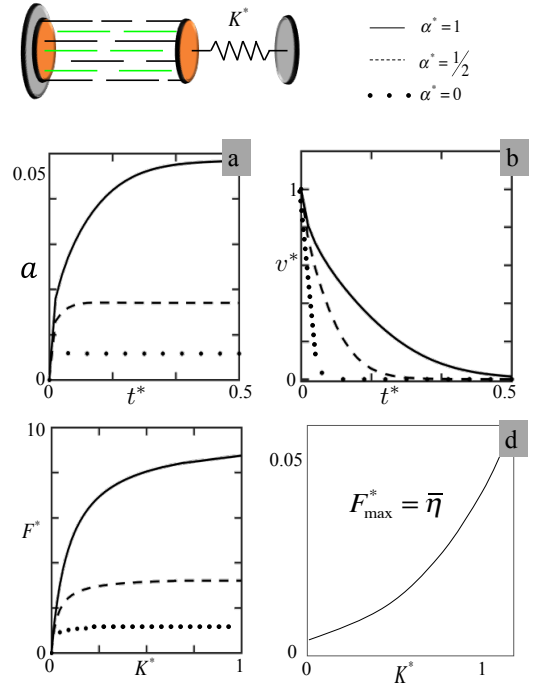


FIG. 5. Investigation of a SF segment as it is contracting against a spring of normalized stiffness $K^* = K/k$ for different values of normalized bond catchiness ($\alpha^* = 0, 0.5$ and 1). **Top figures:** Time evolution of (a) η and (b) shortening velocity $v_s^* = v_s/v_s^0$ for a spring stiffness $K^* = K/k = 0.5$. **Bottom figures:** (c) Relationship between the external stiffness $K^* = K/k$ and the contractile force $F^* = F/\zeta$ applied by the control segment at steady state for different values of bond catchiness α^* . The relationship between maximum contractile force F_{max}^* and bond catchiness is shown in (d).

when $\alpha^* = 0$ (Fig. 5d). The model therefore suggests that the catch-bond behavior is critical for stiffness sensing.

II. FROM STRESS FIBER TO CYTOSKELETON

In the remainder of this work, we scale-up the SF model to the cellular level in order to investigate the effect of the catch-bond hypothesis on the mechano-sensitivity of cells lying on micro-pillars as measured in a number of experimental studies [41–43]. For this, we take $N_f = 20$, $N_x = 10$ in Eq. (1) and assume that the cytoskeleton of an adherent cell initially consists of randomly distributed network of SFs that can anchor at focal adhesion sites, with densities that range between 5 and 15 SF per μm^2 [41, 43] or at the cell periphery (the actin cortex) with a density that range between 5 and 15 per μm [44] (Fig. 6). Although distributed in an isotropic fashion, the length ℓ of each SF is taken to follow an exponential probability distribution given by (Fig. 6c.):

$$\phi(\ell) = \lambda \exp(-\lambda \ell) \quad (13)$$

where $\lambda = 0.2\mu\text{m}$ is known as the rate parameter. We note that this distribution indicates that small SFs can assemble and grow more easily than longer ones, and are thus more likely to be found in the network [45]. Within this structure, the response of SFs follow Eqs. (5), (6) and (7) with the difference that the elastic shortening d_e and the sliding velocity v_s are scaled with the length of each individual SF. The other two important elements of the model are the actin cortex, modeled here as a passive elastic shell surrounding the cytoskeleton and underlying elastic micro-posts, coated with adhesion proteins and to which the stress fibers can adhere at their end sites (Fig. 6b). The motion of these SFs is therefore directly dictated by the mechanical properties of the pillars, determined by their elastic modulus E_p and geometrical properties via classical Euler-Bernoulli theory [41]:

$$F = \left(\frac{3E_p I_p}{h^3} \right) d_p \quad (14)$$

where h is the pillar height, I_p its moment of inertia and d_p the deflection of its tip. For direct comparisons with experiments, we here model cylindrical micro-posts of radius $r = 1.5\mu\text{m}$ ($I_p = r^4/4$) and whose height h can be adjusted to control the effective lateral stiffness. The motion of SFs anchored to the actin cortex similarly follow the displacement of the cortex, as determined by its ability to deform through elastic stretch and bending. Although the cortical membrane is a thin structure that completely surrounds the cell's body, it is approximated here as one-dimensional elastic element delimiting the cell and providing anchor points to SFs. Its deformation is therefore mainly driven by the contraction of attached SF as described in previous studies [46, 47]. For simplicity, we use a small deformation, linear elastic Euler-Bernoulli beam model with elastic modulus $E_c = 20\text{kPa}$ [48, 49], such that the governing equations can be written as [50]:

$$E_c A_c u_{,xx} = 0 \quad (15)$$

$$E_c I_c v_{,xxxx} - q(x, t) = 0 \quad (16)$$

where subscripts $,x$ denote a derivative with respect to the linear distance along the cortex. Furthermore, A_c and I_c are the cross-sectional area and moment of inertia of the cortex, u and v are its axial and transverse displacement respectively while $q(x, t)$ is the distributed load arising from the SF anchored on the cortex (Fig. 6b). Following [51, 52] the flexural stiffness and stretch stiffness are taken to be $1.42 \times 10^{-9} \text{ dyn-cm}$ and $E_c = 20\text{kPa}$, respectively. In what follows, we use a numerical formulation, based on finite elements and whose details are given in appendix, to solve the problem of an adherent cell contracting on a bed of micro-post. In agreement with previous models [53, 54], we assume that neither deformation ($\mathbf{u} = 0$) and nor active stress-fibers ($\eta = 0$) are observed prior to contraction. Furthermore, since the cell cortex is in its minimum energy state prior the contraction, its initial shape can be approximated as a series

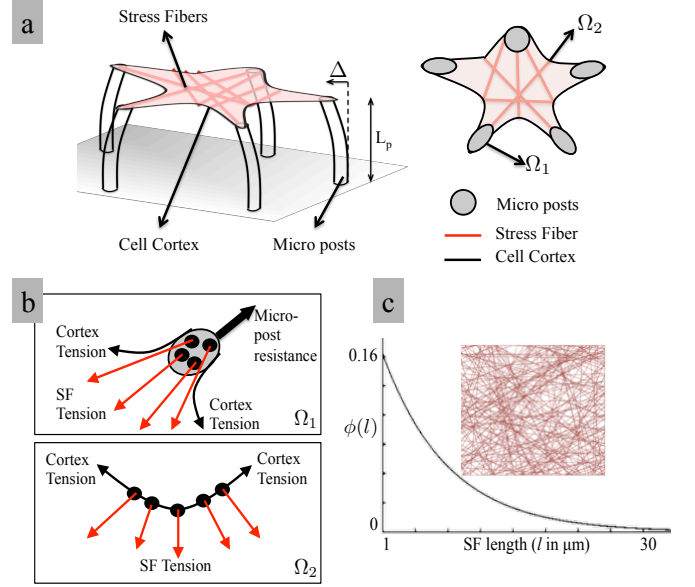


FIG. 6. (a) Schematic of a two-dimensional adherent, cell on micro-posts of length (L_p) within which the contraction of the SF cytoskeleton is balanced with micro-post bending (tip deflection Δ and cortical tension. In the equivalent two-dimensional problem, the anchoring point for SFs are divided into two domains: the tip of micro-posts Ω_1 and the cortical membrane Ω_2 . (b) The micro-posts resist SF traction by providing a reaction expressed by (14) while the cortical tension balances these forces through bending as expressed in (15). (c) In its initial state, the cytoskeleton is modeled with a isotropic and random distribution of SF spanning adhesion points and whose length follow an exponential distribution expressed in (13)

of straight lines between the adhesion sites on the boundary. The nonlinear finite element procedure is then used to compute SF shortening and contractile force (from (5) and (6)) in equilibrium with the surrounding pillars and the cortex at all times as the cell contracts. A steady state is eventually obtained when the force f in all cross-bridges balance the active force ζ .

A. Cellular scale mechanosensitivity

To assess the global mechano-sensitivity of the cytoskeleton, we first numerically reproduce the experimental work described by Tan et al. [41] on smooth muscle cells (BPASMC) in which the cytoskeleton contractility was measured as a function of the overall cell spreading area. For this, our simulations considered square-shaped two-dimensional smooth **muscle** cells (whose properties are given in Table 1) laid on a square lattice of 4, 9 and 16 microposts, respectively. The average contraction force on each pillar was then computed from the micropost deflection (following eq. (14)). A nonlinear relationship was reported between average force and cell area as shown by the average and standard deviation

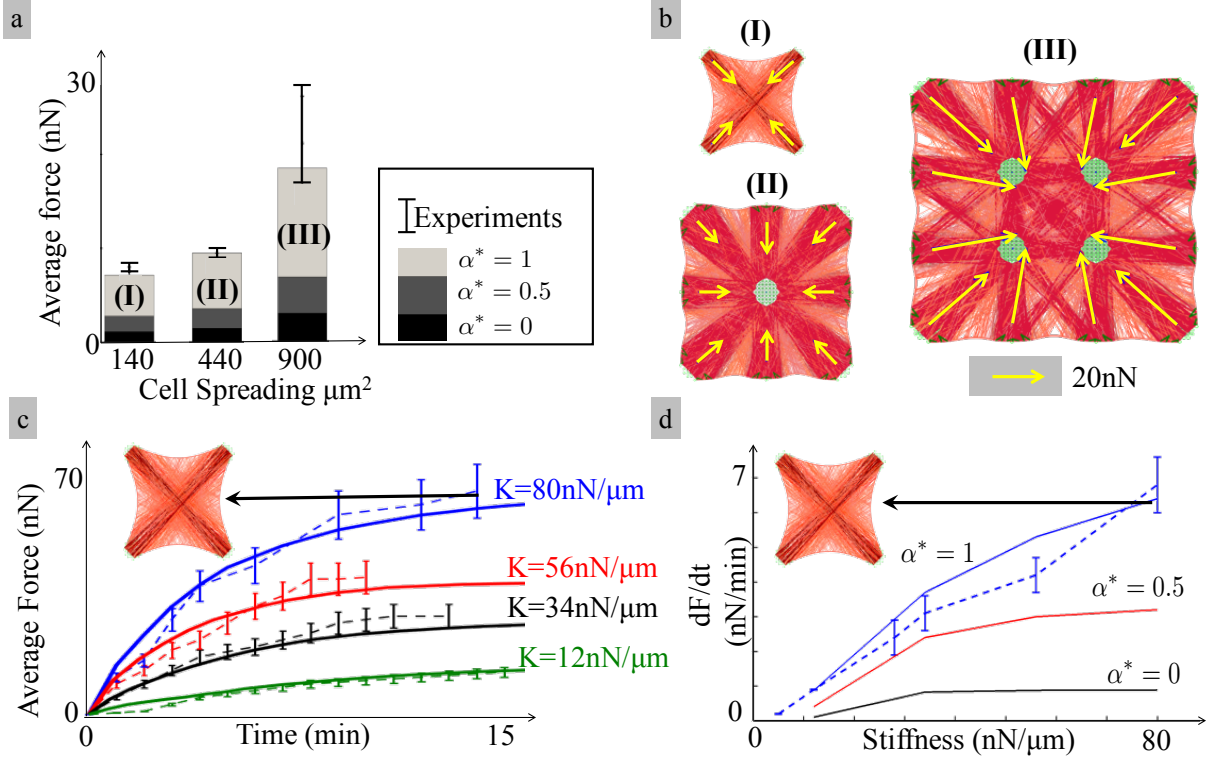


FIG. 7. (a & b) **Effect of cell area on contractility.** (a) Predicted SF distribution for smooth muscle cells (BPASMC) lying on a micropillar substrate consisting of 4, 9 and 16 pillars respectively, all assuming $\alpha^* = 1$. With a fixed pillar radius and spacing of 1.5 and 6 μm , the cell spreading areas are respectively 140, 440 and 900 μm^2 , consistent with experimental conditions presented in the work of Tan et al. The density of anchoring sites for SFs used to match experimental results are respectively 7 per μm^2 on the pillar surfaces and 6 per μm on the cortex. The micropost bending stiffness is 32 nN/ μm [41]. (b) The average force per pillar was computed for the three cell sizes under the hypothesis of an acto-myosin slip bond ($\alpha^* = 0$), moderate catch bond ($\alpha^* = 0.5$) and strong catch bond ($\alpha^* = 1$). The predicted values are compared with experimental results represented by vertical bars (whose positions and lengths depict the mean and standard deviation of the measurements [41]). (c & d) **Dynamics of fibroblast contraction as a function of substrate stiffness.** (c) The evolution of contraction with force was investigated with a square cell lying on four pillars, for which the effective stiffness $K = 3E_p I_p / h^3$ (Eq. (14)) was varied between 12 and 80 nN/ μm . For these simulations, the density of SF anchoring sites was chosen to be 9 per μm^2 on the pillar surface and 12 per μm on the cortex. The curves show the evolution of the contractile force per pillar in time as predicted by the model for $\alpha^* = 1$ (solid lines) and measured experimentally for the fibroblast cells (REF52) investigated in Trichet et al. [43]. (d) Role of bond catchiness on the rate of cell contraction at early times ($t=0$) as a function of micro-post stiffness (K is comprised between 0 and 80 nN/ μm). The dashed line and vertical bars (mean and standard deviation) are experimental data taken from the study of Trichet et al. [43]. The density of SF anchoring sites were chosen as 10 per μm^2 on pillars and 12 per μm on the cortex, respectively while the micropost radius and spacing are 1.5 and 6 μm respectively.

plots in Fig. 7a. In the same figure, we show the simulation results at steady state for the three cells under investigation when an acto-myosin slip bond ($\alpha^* = 0$), a moderate ($\alpha^* = 1/2$) and a strong acto-myosin catch bond ($\alpha^* = 1$) is considered, respectively. The distribution of active SF and cell deformation are also shown for the three cases, all of them in the case $\alpha^* = 1$. Generally, the results show that, once again, bond catchiness is an important factor to mechano-sensitivity and contraction. Indeed, when $\alpha^* = 0$ (slip bond), myosin contraction immediately triggers the detachment of cross-bridges, which results in a near-zero net contraction of the cell as a whole. For increasing bond catchiness however, SF that are locally oriented in directions of large

stiffness (between two attachments, for instance) become activated and are able to apply a contractile force. Furthermore, it became clear from the simulations that while all posts are subjected to pulling forces from SFs, only those close to the cell boundary could undergo significant bending. Indeed, forces are unbalanced on these pillars since no SFs can be found on the external side of the cell, a mechanism is reminiscent of the concept of surface tension between two fluids with different internal cohesive energies. From this observation, one can deduce that cell contraction increases non-linearly with area for two main reasons: (a) for a cell undergoing homogeneous contraction, the deflection of external pillars, and thus measured force, is proportional to its distance

to the center of the cell (in average) and (b) the effective stiffness felt by a SF increases linearly with distance (and thus cell size) according to $K_e = K\ell/2$ (a discussion is provided in the next section). In other words, larger cells behave as if they interacted with a stiffer environment and are thus characterized with a higher contraction (as seen in Fig. 5c). We next evaluate model predictions regarding the transient dynamics response of adherent cells on micro-posts with varying stiffness. For this, we invoke the experimental work of Trichet et al. [43] who explored the time-dependent contractile response of fibroblast (REF52) cells on pillars with effective bending stiffness 12, 34, 56 and $80\text{ nN}/\mu\text{m}$ respectively (Fig. 7b). Generally, contractile forces increased monotonically with time, at a decreasing rate until it reached a plateau, which corresponds to the steady state force. Interestingly, while the overall trends do change with micropost stiffness, the scale of the contractile force does increase significantly with post stiffness. Modeling-wise, these experimental conditions were reproduced by considering a square cell laying on four microposts (see Fig. 7(c&d)) and for which the average post force was computed in time, for the four effective pillar stiffness given above. A comparison of simulations (solid lines) and experimental results (dotted lines) is provided for the case of a strong catch bond. One observes a good match between simulations and experiments for strong catch bond since the stabilization of bond with force allows SF to contract faster (since less force is applied on each bond) and harder (since more cross-bridges are active) when they interact with stiffer substrates while these trends disappear when slip-bonds are considered (as shown in Fig. 5c). This observation was confirmed when we plotted the rate of contraction in terms of substrate stiffness for non-existent, moderate and strong catch bonds as shown in (Fig. 7c). One can clearly see that when $\alpha^* = 0$, the cytoskeleton becomes insensitive to the mechanical properties of its substrate.

B. Mechano-sensitive organization of the cytoskeleton

To conclude our study, we finally investigate how the mechano-sensitive response of a SF segment as described by Eqs. (5) (6) and (7), can give rise to a complex architecture of the actin cytoskeleton observed in most adherent cells. In this context, we simulate the contraction of a fibroblast cell (NIH/3T3) on soft circular pillars as presented by McGarry and coworkers in [12]. The initial cell geometry and underlying pillars are represented in Fig. 8. This geometry was generated by identifying the micro-posts located on the cell boundary from the experimental image and assuming that the cortex is described by straight lines between those posts in its unloaded state. For the simulations, the pillar stiffness was taken to be $80\text{ nN}/\mu\text{m}$ and the cytoskeleton contraction was computed until it reached its steady state value (on the order

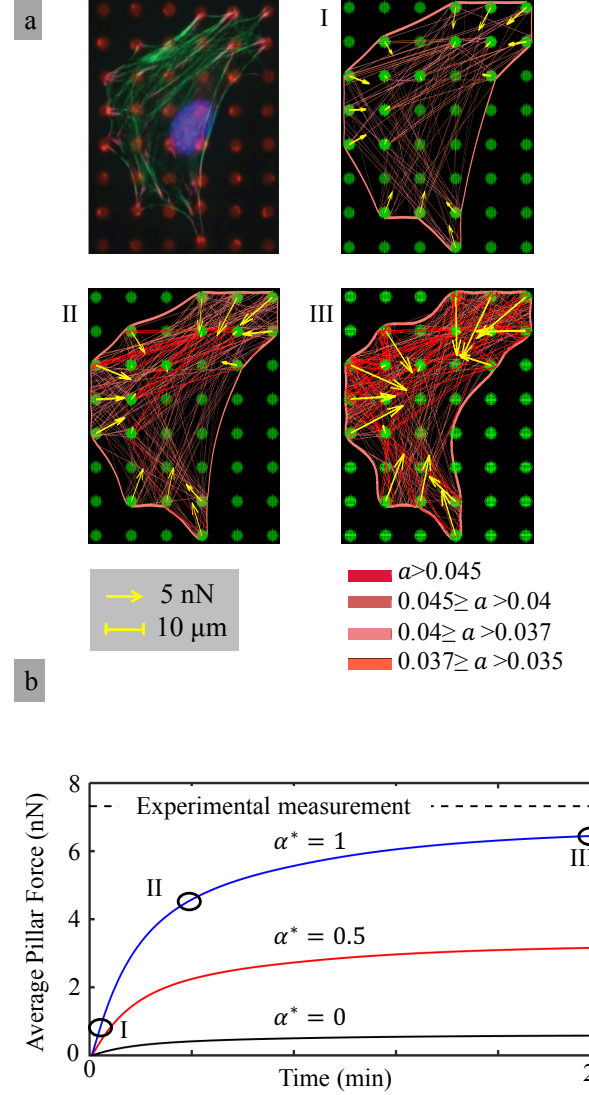


FIG. 8. (a) Time sequence of the SF activation $a = N(\delta_s)\eta/(N_x N_f)$ of a fibroblast cell (NIH/3T3) on micro-post studied by McGarry et al. [12]. The radius, spacing and stiffness of the microposts are 1.5, 10 μm and $80\text{ nN}/\mu\text{m}$ respectively. For this simulation, the density of SF anchoring site was chosen to be 8 per μm^2 on the pillars and 6 per μm on the cortex, respectively. (b) Corresponding average force per pillar shown as a function of time for three types of acto-myosin bonds as characterized by α^* ranging from strong catch bond ($\alpha^* = 1$) to slip bond ($\alpha^* = 0$). Circles correspond to time points I, II and III in (a) while the dashed line shows steady state experimental measurements from [12]

of hundreds of seconds). Fig. 8(I-III) depicts the evolution of the stress fiber activation $a = \eta * N(\delta_s)/(N_x N_y)$, cortex deformation and the corresponding overall force per pillar when the strong catch bond hypothesis is used. Surprisingly, one can see that although smaller SF are predominant as dictated by the distribution Eq.(13), the first SF to activate are the longest. To explain this counterintuitive observation, let us consider two similar SFs

of different lengths, attached to compliant microposts of stiffness K at their ends. The effective stiffness felt by these SFs is then $K_e = F/\epsilon$ where $\epsilon = \Delta\ell/\ell$ is the contractile strain in the SF. For a micropost, the force is related to deflection as $F = K\Delta d$ with $\Delta\ell = 2\Delta d$ and the effective stiffness becomes $K_e = K\ell/2$. In other words, longer SFs effectively sense a larger stiffness than their smaller counterparts, which explains their early activation. Eventually, the deflection of microposts and cortex trigger a larger resisting force causing small SFs to increase their activation level as well. These dynamics result in a sharp increase in SF density and micropost forces and a steady increase of the average pillar force in time. We note that as discussed above, the unbalanced forces on boundaries are responsible for the cortex deformation into curved arches [47] and the large micropost deflection on the edge of the cell. Au contraire, interior pillars, being subjected to more isotropic forces, tend to marginally deform. This restricted deformation in turn, makes interior posts effectively stiffer and prone to adhere to a higher number of SFs. Eventually, the final cytoskeleton organization is strongly dependent on the adhesion pattern, micropost stiffness as well as the overall morphology of the cell. To probe the effect of bond catchiness, we repeated the same simulation for the moderate catch bond ($\alpha^* = 0.5$) and slip bond hypothesis ($\alpha^* = 0$). While the former displays similar trends as for a strong catch bond but with a lesser SF activation and force, the slip bond hypothesis showed, as expected, only marginal contraction and a quasi-nonexistent SF cytoskeleton (Fig. 8b).

III. CONCLUSION

In summary, the role of catch-bonds in cell mechanics is likely to extend far beyond our current knowledge of mechano-sensitive membrane adhesion. Here, we presented a model of acto-myosin interactions within SF structures that shows that the presence of a catch-bond behavior can explain the activation of the cytoskeleton in response to force and stiffness. The model importantly showed that the consideration of catch bond was enough to explain a number of experimental measurements of cell contractility with stiffness and size, in both the static and dynamic regimes. Although the catch bond behavior of acto-myosin was demonstrated ex-vivo [24], the model motivates further experimental studies that can test whether this hypothesis is indeed correct in living systems.

IV. ACKNOWLEDGMENTS

The author would like to acknowledge the support of the National Science Foundation under the CAREER award 1350090 and the National Institute of Health under award 8265940.

V. APPENDIX: NUMERICAL IMPLEMENTATION OF THE MODEL AT THE CELLULAR SCALE

A. A.1. Variational formulation

The cell contraction is governed by three equations given in (5), (6) and (7). One can also estimate the degree of inelastic contraction in a SF as:

$$\Delta d_s(t) = \int_t v_s(t) dt \quad (17)$$

and $\|\mathbf{d}_2 - \mathbf{d}_1\| = \int (\Delta d_s(t) + \Delta d_e) d\ell$ is the total contraction of a SF calculated from the displacements of its two ends \mathbf{d}_1 and \mathbf{d}_2 . In the cellular scale model, the total change in energy of the system $\hat{\mathcal{F}}$ is composed of three components; a contribution \mathcal{F}^{SF} from SFs, a contribution $\dot{\mathcal{E}}^C$ from the cortex deformation and finally, a contribution $\dot{\mathcal{E}}^A$ from the microposts deformation such that:

$$\hat{\mathcal{F}} = \sum_{n=1}^{m_1} \int \mathcal{F}_n d\ell + \int_{\Gamma} \dot{\mathcal{E}}^C d\Gamma + \sum_{n=1}^{m_2} \dot{\mathcal{E}}_n^A \quad (18)$$

where m_1 and m_2 are the total number of SFs in the cell and number of attached pillars respectively. The first term is the integration of the free energy of SFs over their respective lengths ℓ , the second term is the integration of the internal energy of cortex over the boundary Γ while the last correspond to the bending energy of the microposts. Note that the work done by an external force is comprised in the first term such that it is equal to the integration of the external forces over the cell boundary Γ :

$$\sum_{n=1}^{m_1} \int (F_e \delta \Delta d_e) d\ell = \int_{\Gamma} \mathbf{f}^{ext} \cdot \delta \mathbf{d} d\Gamma \quad (19)$$

where \mathbf{f}^{ext} being the force vector on the cell boundary and \mathbf{d} the associated displacement field. The stored elastic (bending) energy \mathcal{E}_n^A in a micropost reads:

$$\mathcal{E}_n^A = \frac{1}{2} \left(\frac{3E_p I_p}{h^3} \right) (d_p^n)^2 \quad (20)$$

where d_p^n is the total deflection of the n^{th} micropost which is equal to the resultant of the displacement field $d_p = (d_x^2 + d_y^2)^{(1/2)}$ and d_x, d_y are the horizontal and vertical components of the displacement vector (in our predefined orthonormal coordinate system). The work contribution from the cortex finally originates from both axial deformation and bending; assuming that these modes of deformation are uncoupled, one can write \mathcal{E}_n^C :

$$\begin{aligned} \mathcal{E}^C = & \frac{1}{2} \int_{\Gamma} \frac{\partial d_{\parallel}}{\partial x_{\parallel}} (E_c A_c) \frac{\partial d_{\parallel}}{\partial x_{\parallel}} dx_{\parallel} \\ & + \frac{1}{2} \int_{\Gamma} \frac{\partial^2 d_{\perp}}{\partial x_{\parallel}^2} (E_c I_c) \frac{\partial^2 d_{\perp}}{\partial x_{\parallel}^2} dx_{\parallel} \end{aligned} \quad (21)$$

where $d_{\parallel} = \mathbf{d}_c \cdot (\mathbf{1} - \mathbf{n})$ and $d_{\perp} = \mathbf{d}_c \cdot \mathbf{n}$ are the axial and transverse components of cortex deformation and \mathbf{n} is the unit normal of the corresponding cortex segment with a length L_c . The integral of the cell cortex is over its axial direction x_{\parallel} (see Fig. 9). Since SF are assumed to not separate from adhesion complexes, the displacement field of the system can be written in terms of those of cortex $\mathbf{d} = \mathbf{d}_c$ and pillars $\mathbf{d} = \mathbf{d}_p$. Based on variational principles total work functional can be written as:

$$(\delta_{\mathbf{d}} \hat{\mathcal{F}}) \delta \mathbf{d} + (\delta_{\eta} \hat{\mathcal{F}}) \delta \eta + (\delta_{v_s} \hat{\mathcal{F}}) \delta v_s = 0 \quad (22)$$

This ultimately leads to:

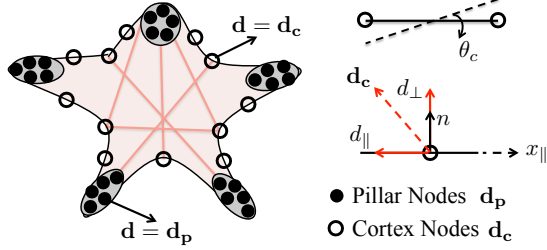


FIG. 9. Schematic of the assembly of the comprising elements; cortex, pillars and SF's. There are nodes only on the cell boundary, which are shared by either SF-cortex or SF pillar coupling.

$$\begin{aligned} & \left(\sum_{n=1}^{m_1} \int (\delta \Delta d^n) \eta \Delta d^n N k d\ell \right) + \left(\sum_n^{m_2} (\delta d_p^n) \left(\frac{3E_p I_p}{L_p^3} \right) d_p^n \right) \\ & + \int_{\Gamma} \left(\frac{\partial \delta d_{\parallel}}{\partial x_{\parallel}} (E_c A_c) \frac{\partial d_{\parallel}}{\partial x_{\parallel}} + \frac{\partial^2 \delta d_{\perp}}{\partial x_{\parallel}^2} (E_c I_c) \frac{\partial^2 d_{\perp}}{\partial x_{\parallel}^2} \right) dx_{\parallel} \\ & - \left(\sum_{n=1}^{m_1} \int (\delta \Delta d) \eta \Delta d_s(t) N k d\ell \right) + \left(\int_{\Gamma} (\delta d) \mathbf{f}^{ext} d\Gamma \right) = 0 \end{aligned} \quad (23)$$

$$\sum_{n=1}^{m_1} \int (\delta \eta) \left(E_b + k_B T \ln \left(\frac{\eta}{1 - \eta} \right) \right) d\ell = 0 \quad (24)$$

$$\sum_{n=1}^{m_1} \int (\delta v_s) \left(-v_s/v_s^0 + 1 - k(\Delta d - \Delta d_s(t))/\zeta \right) d\ell = 0 \quad (25)$$

where the assembly operator \mathcal{A}_I establishes the connection between the index of each SF and the index of their connection with the cortex of micro-posts. This concept is well known in the finite-element literature.

B. A.2. Finite element implementation

In the proposed model, SF reach a pseudo-equilibrium state when the variation of the work $\hat{\mathcal{F}}$ is minimized with

respect to the field variables comprised of two displacements (d_x and d_y where $d^2 = d_x^2 + d_y^2$), rotation of the cortex segments θ_c , activation parameter η the contraction d_s and its rate v_s . Here we introduced a new variable θ_c (defined as the first derivative of the transverse displacement with respect to the axial direction, $\theta_c = \partial d_{\perp} / \partial x_{\parallel}$) in order to satisfy the continuity of the cortex deformation. The rotation can be written as $\tan^{-1}(2d_{\perp}/L_c)$ for a discrete cortex segment, and assuming that rotations are small $\theta_c \approx (2d_{\perp}/L_c)$. The balance equations (23), (24) and (25) are collected in a residual form as a function of the variables:

$$\mathbf{R}(\mathbf{x}, t) = 0 \quad \text{where} \quad \mathbf{x} = [u_x \ u_y \ \theta_c \ \eta \ v_s].$$

The linearized form of the system of equations is obtained as follows:

$$\frac{\partial \mathbf{R}(\mathbf{x}, t)}{\partial \mathbf{x}} \delta \mathbf{x} + \mathbf{R}(\mathbf{x}, t) = 0. \quad (26)$$

A numerical solution of this equation is obtained using the finite element (FE) method. From this view point, we use simple structural elements to model SFs, frame elements to describe the cell cortex [50] and connector elements for the connection between SFs and adhesion sites (to enforce the no separation condition with the penalty method). The equilibrium solution is then found using a standard Newton-Raphson iterative procedure in the form:

$$\begin{aligned} \delta \mathbf{x}^k &= -(\mathbf{K}(\mathbf{x}^k))^{-1} \mathbf{R}(\mathbf{x}^k) \\ \mathbf{x}^{k+1} &= \mathbf{x}^k + \delta \mathbf{x}^k \end{aligned} \quad (27)$$

where $\mathbf{K}(\mathbf{x}) = \partial \mathbf{R}(\mathbf{x}) / \partial \mathbf{x}$. Regarding the FE interpolation, we use linear shape functions \mathbf{N} for displacement, Hermitian shape functions \mathbf{H} for the cortex rotation and transverse displacement and constant shape functions for both activation and contraction rate as follows:

$$\begin{aligned} w_1 &= \mathbf{N} \mathbf{w} = [N_1 \ N_2] \mathbf{w} \\ w_2 &= \mathbf{H} \mathbf{w} = [H_1 \ H_2 \ H_3 \ H_4] \mathbf{w} \\ w_3 &= w \end{aligned}$$

where $N_1(\xi) = (1 - \xi)/2$, $N_2(\xi) = (1 + \xi)/2$, $H_1(\xi) = 1 - 3\xi^2/l^2 + 2\xi^3/l^3$, $H_2(\xi) = \xi - 2\xi^2/l + \xi^3/l^2$, $H_3(\xi) = 3\xi^2/l^2 - 2\xi^3/l^3$ and $H_4(\xi) = -\xi^2/l + \xi^3/l^2$, ξ being the coordinate in a parametric space comprised between -1 and 1. For the mechanics part of the problem stiffness matrix \mathbf{K} takes the form:

$$\begin{aligned} \mathbf{K}_{mm} &= \mathcal{A}_I \int \mathbf{T}^T \frac{d\mathbf{N}^T}{dx} N(\Delta d_s^n) \eta^n k \frac{d\mathbf{N}}{dx} \mathbf{T} d\ell \\ & \quad \mathcal{A}_I \mathbf{T}^T \frac{d\mathbf{N}^T}{dx} \left(\frac{3E_p I_p}{h^3} \right) \frac{d\mathbf{N}}{dx} \mathbf{T} \\ & \quad \mathcal{A}_I \left[\int_{d\Gamma} \mathbf{T}^T \frac{d\mathbf{N}^T}{dx} (E_c A_c) \frac{d\mathbf{N}}{dx} \mathbf{T} \right. \\ & \quad \left. + \left(\hat{\mathbf{T}}^T \frac{d^2 \mathbf{H}^T}{dx^2} (E_c I_c) \frac{d^2 \mathbf{H}}{dx^2} \hat{\mathbf{T}} \right) d\Gamma \right] \end{aligned}$$

where

$$\mathbf{K}_{mm} = \begin{bmatrix} \mathbf{K}_{u_1 u_1} & \mathbf{K}_{u_1 u_2} & \mathbf{K}_{u_1 \theta_c} \\ \mathbf{K}_{u_2 u_1} & \mathbf{K}_{u_2 u_2} & \mathbf{K}_{u_2 \theta_c} \\ \mathbf{K}_{\theta_c u_1} & \mathbf{K}_{\theta_c u_2} & \mathbf{K}_{\theta_c \theta_c} \end{bmatrix}.$$

The transformation matrices (\mathbf{T} and $\hat{\mathbf{T}}$) from local to global are:

$$\mathbf{T} = \begin{bmatrix} c & s & 0 & 0 \\ 0 & 0 & c & s \end{bmatrix}, \quad \hat{\mathbf{T}} = \begin{bmatrix} \mathbf{R} & \mathbf{0} \\ \mathbf{0} & \mathbf{R} \end{bmatrix} \quad \text{where } \mathbf{R} = \begin{bmatrix} c & s & 0 \\ -s & c & 0 \\ 0 & 0 & 1 \end{bmatrix}$$

where $c = \cos(\theta)$ and $s = \sin(\theta)$. For the force-activation coupling the stiffness matrix term is:

$$[\mathbf{K}_{u_1 \eta}^T \quad \mathbf{K}_{u_2 \eta}^T]^T = \mathcal{A}_I \int \left(\mathbf{T}^T \frac{d\mathbf{N}^T}{dx} N(\Delta d_s^n) k \frac{d\mathbf{N}}{dx} \mathbf{T} \mathbf{u} \right) d\ell.$$

The stiffness tangent for the activation parameter is:

$$\mathbf{K}_{\eta \eta} = \left[\int \left(k_B T \frac{1}{\eta - \eta^2} \right) d\ell \right]$$

and its coupling with the force on the SF is:

$$[\mathbf{K}_{\eta u_1} \quad \mathbf{K}_{\eta u_2}] = \left[\mathcal{A}_I \int \left((\alpha(\exp(-f/f_0)) - \Delta x) k \frac{d\mathbf{N}}{dx} \mathbf{T} \right) d\ell \right].$$

And finally the stiffness tangent term for the dissipation is:

$$\mathbf{K}_{v_s v_s} = \mathcal{A}_I \int -1/v_s^0 d\ell$$

$$[\mathbf{K}_{v_s u_1} \quad \mathbf{K}_{v_s u_2}] = \left[\mathcal{A}_I \int \left(\mathbf{T}^T \frac{d\mathbf{N}^T}{dx} \frac{-k}{\zeta} \frac{d\mathbf{N}}{dx} \mathbf{T} \mathbf{u} \right) d\ell \right].$$

The final form is:

$$\mathbf{K} = \begin{bmatrix} \mathbf{K}_{u_1 u_1} & \mathbf{K}_{u_1 u_2} & \mathbf{K}_{u_1 \theta_c} & \mathbf{K}_{u_1 \eta} & \mathbf{K}_{u_1 v_s} \\ \mathbf{K}_{u_2 u_1} & \mathbf{K}_{u_2 u_2} & \mathbf{K}_{u_2 \theta_c} & \mathbf{K}_{u_2 \eta} & \mathbf{K}_{u_2 v_s} \\ \mathbf{K}_{\theta_c u_1} & \mathbf{K}_{\theta_c u_2} & \mathbf{K}_{\theta_c \theta_c} & \mathbf{0} & \mathbf{0} \\ \mathbf{K}_{\eta u_1} & \mathbf{K}_{\eta u_2} & \mathbf{0} & \mathbf{K}_{\eta \eta} & \mathbf{0} \\ \mathbf{K}_{v_s u_1} & \mathbf{K}_{v_s u_2} & \mathbf{0} & \mathbf{0} & \mathbf{K}_{v_s v_s} \end{bmatrix}.$$

After solving the system of equations one can calculate the total contraction as:

$$d_s(t^{k+1}) = d_s(t^k) + v_s(t^{k+1})dt.$$

An overview of the computational algorithm is given in Fig. 10

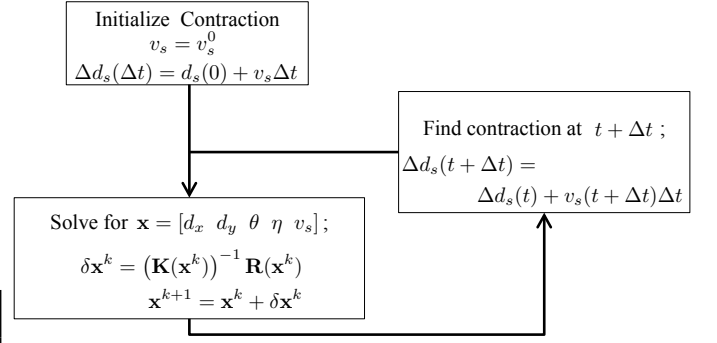


FIG. 10. Algorithm used to solve (23), (24) and (25).

C. A.3. Model parameters and differences between non-muscle myosin and smooth muscle myosin.

A summary of the model parameters used in our study is given in Table 1. We note here that there exists some significant differences in the properties of myosin heads based on their types.

Kinetics: In the literature, it is reported that the sliding velocity of myosin heads ranges from 0.05 [58, 59] to 2 $\mu\text{m/s}$ [29] in non-muscle myosin II and from 0.3 [60] to 0.8 $\mu\text{m/s}$ [61] for smooth muscle myosin. In this study, we have only investigated the dynamical behavior of NMM (Fig. 7(c&d) and Fig. 8) for which a sliding velocity $v = 1 \mu\text{m/s}$ was selected consistent with experimental measurements in fibroblasts [29]. We note here that results on smooth muscle cells presented in Fig. 7(a&b) are at steady state and thus independent of the chosen value of sliding velocity. Nevertheless, for those cells, our model would predict contraction-time relationships that are similar to those presented in Fig. 7c but characterized by different time scales (due to differences in sliding velocities [29, 59, 62]).

Mechanical Properties: Regarding the mechanical properties, cross-bridge stiffness for the skeletal muscle cells ranges from 130 [63] to 2400 $\text{pN}/\mu\text{m}$ [64–66]. In the literature, there is a lack of data about the acto-myosin bond stiffness for the smooth muscle and non-muscle cells investigated in this paper. In order to be consistent with previous studies [28, 57], we however chose this stiffness to be 600 $\text{pN}/\mu\text{m}$ throughout the investigation of cellular mechano-sensitivity. Although our selection may be inaccurate in certain cases, we note from Fig. 11b that the effect of cross-bridge stiffness on the rate of contractile force is insignificant.

Catch bond properties: We used the catch bond data of skeletal muscle cells due to the lack of experimental data for both non-muscle and smooth muscle cells. Our choice for the critical force (f_c) of 6 pN , however, does not affect the trends of the catch bond behavior. This choice would only change the maximum load that a

TABLE I. Parameters for the SF model

| Parameter | Meaning | Value |
|------------|--------------------------------------|---------------------------------------|
| Δx | Width of the energy barrier | 3 nm [39] |
| f_0 | Normalizing force | 2.2 pN |
| E_0 | Reference energy of catch bond | 1.98×10^{-19} J |
| α | Bond catchiness | $2.4 k_B T$ |
| N_x | Number of myosin heads per filament | 20 [17] |
| N_f | Number of myosin filament per bundle | 10 [55, 56] |
| l | Length of the control segment | $1 \mu\text{m}$ [55, 56] |
| T | Absolute temperature | 300K |
| ζ | Stall force | 5pN [37] |
| k | Actomyosin bond elasticity | $600 \text{ pN}/\mu\text{m}$ [28, 57] |
| v | Maximum contraction velocity of SF | $1 \mu\text{m}/\text{s}$ [29] |

SF can carry and would change the SF density at the cellular level. As the critical force f_c reduces, the SF density in the cell should increase in order to match experimental data [43].

D. A.4. Effect of acto-myosin bond stiffness on mechanosensing

The reported data on the acto-myosin bond stiffness is limited to skeletal muscle cells from different animals (rabbit and frog). It is furthermore very scattered; for instance, measured values for rabbit skeletal muscle cells range from $130 \text{ pN}/\mu\text{m}$ [63] to $1700 \pm 700 \text{ pN}/\mu\text{m}$ [64, 65] while it has been estimated to be between $1000 - 2200 \text{ pN}/\mu\text{m}$ [66] for frog. Because of this variability, we propose here to perform a parametric study to better understand the effect of bond stiffness k on mechanosensitivity and contraction dynamics, as predicted by the model in the case of a strong catch bond ($\alpha^* = 1$). We chose three stiffness values $k = 10, 100, 2000 \text{ pN}/\mu\text{m}$ and investigated the SF response under the virtual experimental setup presented in Fig. 5. In the results reported in Fig. 11, one sees that acto-myosin bond stiffness affects both the SF sensitivity to external stiffness and the rate of SF activation. Fig. 11a indeed shows that the contractile force of the SF becomes weaker as k decreases, such that when $k = 10 \text{ pN}/\mu\text{m}$, a quasi-inexistent contraction is observed. This follows from the fact that highly compliant cross-bridges can only apply little force even in the case of large contraction strains. Fig. 11b further shows that the rate of SF activation a increases with

bond stiffness. However, regardless of bond stiffness, we observed that the key trends exhibited by the model are always consistent both at the SF and at the cellular level. In other words, bond stiffness and SF density can always be adjusted accordingly to match model predictions and experimental measurements at the cellular level, without modifying the trends shown in this paper. This motivated our choice of fixed value $k = 600 \text{ pN}/\mu\text{m}$ for our simulations.

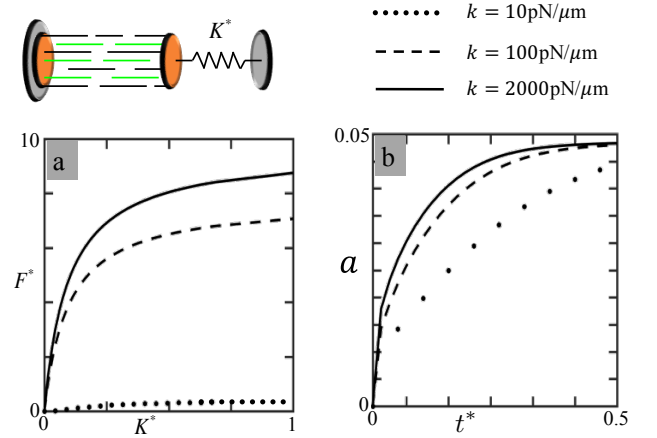


FIG. 11. Parametric study of acto-myosin bond stiffness ($k = 10, 100$ and $2000 \text{ pN}/\mu\text{m}$ using the control segment connected to a linear spring. (a) Normalized contractile force $F^* = F/\zeta$ as a function of normalized external stiffness $K^* = K/2000$. One sees that the stiffness sensing ability of the SF's increases with bond stiffness k . (b) Activation parameter a versus time for $K^* = 0.5$. The rate of crossbridge activation also increases with bond stiffness k .

- [1] S. C. Baxter, M. O. Morales, and E. C. Goldsmith, Cell Biochemistry and Biophysics **51**, 33 (2008).
- [2] I. B. Bischofs and U. S. Schwarz, Proceedings of the Na-

tional Academy of Sciences of the United States of America **100**, 9274 (2003).

- [3] D. E. Discher, P. Janmey, and Y. li Wang, Science **310**,

- 1139 (2005).
- [4] U. S. Schwarz and I. B. Bischofs, *Medical Engineering and Physics* **27**, 763 (2005).
 - [5] P. Fernandez and A. R. Bausch, *Integrative Biology* **1**, 252 (2009).
 - [6] T. M. Freyman, I. V. Yannas, R. Yokoo, and L. J. Gibson, *Biomaterials* **22**, 2883 (2001).
 - [7] H. B. Wang, M. Dembo, and Y. Wang, *American Journal of Physiology Cell Physiology* **279**, C1345 (2000).
 - [8] J. Solon, I. Levental, K. Sengupta, P. C. Georges, and P. Janmey, *Biophysical Journal* **93**, 4453 (2007).
 - [9] F. Vernerey and M. Farsad, *Journal of mathematical biology* **68**, 989 (2013).
 - [10] U. S. Schwarz and S. A. Safran, *Physical Review Letters* **88**, 048102 (2002).
 - [11] I. B. Bischofs, S. A. Safran, and U. S. Schwarz, *Physical Review E* **69**, 021911 (2004).
 - [12] J. P. McGarry, J. Fu, M. T. Yang, C. S. Chen, R. M. McMeeking, A. G. Evans, and V. S. Deshpande, *Philosophical Transactions of the Royal Society of London A: Mathematical, Physical and Engineering Sciences* **367**, 3477 (2009).
 - [13] L. Foucard and F. Vernerey, *Applied Physics Letters* **100** (2011), 10.1063/1.3673551.
 - [14] F. J. Vernerey and M. Farsad, *Journal of the mechanical behavior of biomedical materials* **4**, 1683 (2011).
 - [15] V. S. Deshpande, R. M. McMeeking, and A. G. Evans, *Proceedings of the National Academy of Science* **103**, 14015 (2006).
 - [16] A. F. Huxley, *Progress in Biophysics and Biophysical Chemistry* **7**, 255 (1957).
 - [17] R. Kaunas, H. Hsu, and S. Deguchi, *Cell Health and Cytoskeleton* **3**, 13 (2011).
 - [18] U. S. Schwarz and S. A. Safran, *Reviews of Modern Physics* **85** (2013).
 - [19] B. T. Marshall, M. Long, J. W. Piper, T. Yago, R. P. McEver, and C. ZhuD, *Letters to Nature* **423**, 190 (2003).
 - [20] E. Novikova and C. Storm, *Biophysical journal* **105**, 1336 (2013).
 - [21] G. I. Bell, *Science* **200**, 618 (1978).
 - [22] W. E. Thomas, V. Vogel, and E. Sokurenko, *Annual review of biophysics* **37**, 399 (2008).
 - [23] W. Thomas, *Annual review of biomedical engineering* **10**, 39 (2008).
 - [24] B. Guo and W. H. Guilford, *Proceedings of the National Academy of Sciences of the United States of America* **103**, 9844 (2006).
 - [25] M. Capitanio, M. Canepari, M. Maffei, D. Beneventi, M. Monico, F. Vanzi, R. Bottinelli, and F. Pavone, *Nature Methods* **9**, 1013 (2012).
 - [26] M. Reconditi, M. Linari, L. Lucii, A. Stewart, Y. Sun, P. Boesecke, T. Narayanan, R. Fischetti, T. Irving, G. Piazzesi, M. Irving, and V. Lombardi, *Nature* **428**, 578 (2004).
 - [27] G. Langanger, M. Moeremans, G. Daneels, A. Sobieszek, M. D. Brabander, and J. D. Mey, *J Cell Biol.* **102**, 200 (1986).
 - [28] P. Fernández, P. A. Pullarkat, and A. Ott, *Biophysical Journal* **90**, 3796 (2006).
 - [29] K. Katoh, Y. Kano, M. Masuda, H. Onishi, and K. Fujiwara, *Molecular Biology of the Cell* **9**, 1919 (1998).
 - [30] A. M. Gordon, A. F. Huxley, and F. Julian, *Journal of Physiology* **184**, 170 (1966).
 - [31] C. Hai and R. A. Murphy, *American Journal of Physiology* **254**, C99 (1988).
 - [32] B. Brook and O. Jensen, *Mathematical Medicine and Biology* **31**, 99 (2014).
 - [33] C. Dong and B. Chen, *Nature* doi:10.1038/srep19506 (2016).
 - [34] B. Chen, *Journal of Applied Mechanics* **80**, 1 (2013).
 - [35] F. Julicher, K. Kruse, J. Prost, and J. Joanny, *Physics Reports* **449**, 3 (2007).
 - [36] A. Hill, *Proc. R. Soc. Lond. B. Biol. Sci.* **216**, 136 (1938).
 - [37] S. Chaen, J. Inoque, and H. Sugi, *The Journal of Experimental Biology* **198**, 1021 (1995).
 - [38] Y. V. Pereverzev and O. V. Prezhdho, *Physical Review E* **73**, 050902 (2006).
 - [39] E. Evans, *Annu. Rev. Biophys. Biomol. Struct* **30**, 105 (2001).
 - [40] B. Chakrabarti and L. G. Benguigui, *Statistical Physics of Fracture and Breakdown in Disordered Systems* (Oxford: Clarendon Press, 1997).
 - [41] J. L. Tan, J. Tien, D. M. Pirone, D. S. Gray, K. Bhadriraju, and C. S. Chen, *Proceedings of the National Academy of Science* **100**, 1484 (2002).
 - [42] M. Ghibaudo, A. Saez, L. Trichet, A. Xayaphoummine, J. Browaeys, P. Silberzan, A. Buguin, and B. Ladoux, *Soft Matter* **4**, 1836 (2008).
 - [43] L. Trichet, J. LeDigabel, R. J. Hawkins, S. R. K. Vedula, M. Gupta, C. Ribault, P. Hersen, R. Voituriez, and B. Ladoux, *Proceedings of the National Academy of Sciences of the United States of America* **109**, 6933 (2012).
 - [44] S. Walcott and S. X. Sun, *Proceedings of the National Academy of Science* **107**, 7757 (2009).
 - [45] M. Thery, A. Pepin, E. Dressaire, Y. Chen, and M. Bornens, *Cell Motility and the Cytoskeleton* **63**, 341 (2006).
 - [46] I. Bischofs, F. Klein, D. Lehnert, M. Bastmeyer, and U. Schwarz, *Biophysical Journal* **95**, 3488 (2008).
 - [47] F. Vernerey and M. Farsad, *Computer Methods in Biomechanics and Biomedical Engineering* **14**, 433 (2011).
 - [48] H. Dailey, L. M. Ricles, H. C. Yalcin, and S. N. Ghadiali, *Journal of Applied Physiology* **106**, 221 (2008).
 - [49] R. Vargas-Pinto, H. Gong, A. Vahabikashi, and M. Johnson, *Biophysical Journal* **105**, 300 (2013).
 - [50] Y. W. Kwon and H. Bang, *The Finite Element Method Using MATLAB* (CRC, 2000).
 - [51] R. Vargas-Pinto, H. Gong, A. Vahabikashi, and M. Johnson, *Biophysical Journal* **105**, 300 (2013).
 - [52] H. Dailey, L. Ricles, H. Yalcin, and S. Ghadiali, *Journal of Applied Physiology* **106**, 221 (2009).
 - [53] F. J. Vernerey and M. Farsad, *Journal of Mathematical Biology* **68**, 989 (2014).
 - [54] E. P. Dowling, W. Ronan, G. Ofek, V. S. Deshpande, R. M. McMeeking, K. A. Athanasiou, and J. P. McGarry, *Journal of the Royal Society of Interface* **9**, 3469 (2012).
 - [55] S. Pellegrin and H. Mellor, *Journal of cell science* **120**, 3491 (2007).
 - [56] S. Tojkander, G. Gateva, and P. Lappalainen, *Journal of cell science* **125**, 1855 (2012).
 - [57] J. Howard, *Mechanics of motor proteins*, edited by F. Flyvbjerg, F. Julicher, P. Ormos, and F. David, 75 (Springer Berlin Heidelberg, 2002).
 - [58] K.-Y. Kim, M. Kovács, S. Kawamoto, J. R. Sellers, and R. S. Adelstein, *The Journal of Biological Chemistry* **280**, 22769 (2005).
 - [59] F. Wang, M. Kovacs, A. Hu, J. Limouze, E. V. Harvey,

- and J. R. Sellers, *The Journal of Biological Chemistry* **278**, 27439 (2003).
- [60] D. M. Warshaw, J. M. Desrosiers, S. S. Work, and K. M. Trybus, *The Journal of Cell Biology* **111**, 453 (1990).
- [61] D. E. Harris, S. S. Work, R. K. Wright, N. R. Alpert, and D. M. Warshaw, *Journal of Muscle Research & Cell Motility* **15**, 11 (1994).
- [62] G. Cuda, E. Pate, R. Cooke, and J. R. Sellers, *Biophysical Journal* **72**, 1767 (1997).
- [63] J. E. Molloy, J. E. Burns, J. C. Sparrow, R. T. Tregear, J. Kendrick-Jones, and D. C. White, *Biophysical Journal* **68**, 298S (1995).
- [64] M. Linari, M. Caremani, C. Piperio, P. Brandt, and V. Lombardi, *Biophysical Journal* **92**, 2476 (2007).
- [65] A. Lewalle, W. Steffen, O. Stevenson, Z. Ouyang, and J. Sleep, *Biophysical Journal* **94**, 2160 (2008).
- [66] C. J. Barclay, *Journal of Muscle Research & Cell Motility* **19**, 855 (1998).